

## Full Length Article

# The effect of manufacturing defects on compressive strength of ultralight hollow microlattices: A data-driven study



L. Salari-Sharif<sup>a,c</sup>, S.W. Godfrey<sup>b</sup>, M. Tootkaboni<sup>c</sup>, L. Valdevit<sup>a,\*</sup>

<sup>a</sup> Mechanical and Aerospace Engineering Department, University of California, Irvine, United States

<sup>b</sup> Computer Science Department, University of California, Irvine, United States

<sup>c</sup> Civil and Environmental Engineering Department, University of Massachusetts, Dartmouth, United States

## ARTICLE INFO

## Article history:

Received 24 December 2016

Received in revised form 8 October 2017

Accepted 2 November 2017

Available online 8 November 2017

## Keywords:

Ultralight microlattice

Manufacturing defects

Compressive strength

Geometric imperfections

Data-driven stochastic analysis

## ABSTRACT

Hollow microlattices constitute a model topology for architected materials, as they combine excellent specific stiffness and strength with relative ease of manufacturing. The most scalable manufacturing technique to date encompasses fabrication of a sacrificial polymeric template by the Self Propagating Photopolymer Waveguide (SPPW) process, followed by thin film coating and removal of the substrate. Accurate modeling of mechanical properties (e.g., stiffness, strength) of hollow microlattices is challenging, primarily due to the complex stress state around the hollow nodes and the existence of manufacturing-induced geometric imperfections (e.g. cracks, non-circularity, etc.). In this work, we use a variety of measuring techniques (SEM imaging, CT scanning, etc.) to characterize the geometric imperfections in a nickel-based ultralight hollow microlattice and investigate their effect on the compressive strength of the lattice. At the strut level, where a more quantitative description of geometric defects is available, the gathered data is used to build a stochastic field model of geometric imperfections using Proper Orthogonal Decomposition. Using Monte Carlo simulations, the critical buckling loads of a large set of imperfect bars created using the stochastic model are then extracted by Finite Elements Analysis. The statistics of the buckling strength in artificially generated bars is then used to explain the scatter in the strength of CT-derived bars and its correlation with the lattice strength measured experimentally. Although the quantitative results are specific to microlattices fabricated by SPPW templating, the methodology presented herein is equally applicable to architected materials produced by other manufacturing processes.

© 2017 Elsevier B.V. All rights reserved.

## 1. Introduction

Over the past two decades, architected materials have received substantial attention due to their unique mechanical, electrical, thermal, and acoustic properties [1,2]. In particular, architected materials achieve combinations of properties that are unattainable by their monolithic constituent materials: examples include combinations of low density and high stiffness [3], low density and high strength [4], high energy absorption and low strength [5–7], and high active cooling performance at low pressure drop [8].

Recently, a number of novel manufacturing techniques have been proposed which enable fabrication of macro-scale architected materials with carefully controlled micro and nano-scale features at the unit and sub-unit cell level [9,10]. These architected mate-

rials take advantage of beneficial micro/nano-size effects on the mechanical properties of their constituent materials to achieve extreme mechanical performance at the macro-scale [11].

Among architected materials, hollow microlattices have emerged as model topologies, due to the availability of reasonably scalable fabrication techniques that allow a structural hierarchy that spans over 7 orders of magnitude (from cm to nm), and the relative simplicity of their mechanical modeling [9,12,13]. The most scalable manufacturing process for this class of materials consists of fabricating a sacrificial polymeric template via a novel self-propagating photopolymer waveguide process (SPPW) [14,15], and coating this template with a thin structural film (generally a metal, but possibly a polymer or a ceramic). The polymeric template is ultimately removed by an etching approach. Previous studies on strength and stiffness of metallic microlattices produced with this technique [16–18] have shown that the experimentally measured stiffness and strength are always significantly lower than predicted by analytical and numerical models,

\* Corresponding author.

E-mail address: [valdevit@uci.edu](mailto:valdevit@uci.edu) (L. Valdevit).

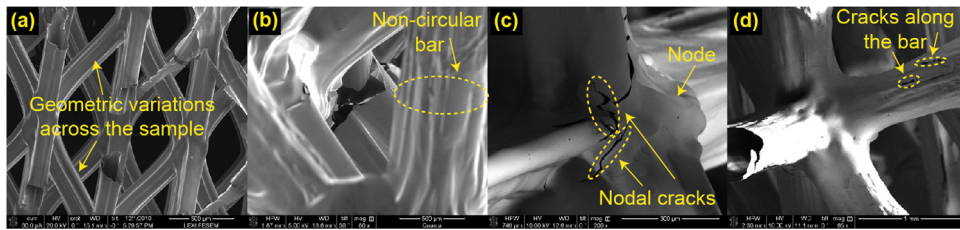


**Fig. 1.** Typical geometric defects observed in hollow metallic microlattice materials produced with the SPPW process: (a) geometric properties variations across the sample; (b) non-circular cross section of the bars; (c) geometric imperfections at nodes and nodal cracks; (d) cracks along the bars.

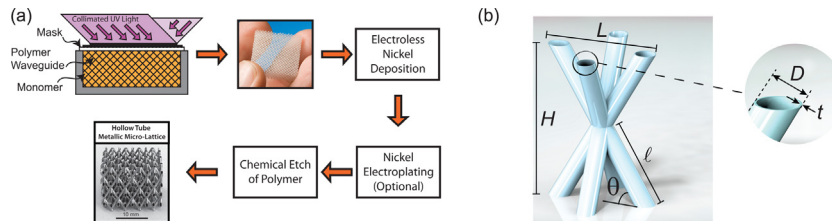


**Fig. 2.** (a) SPPW-based manufacturing process for nickel hollow microlattice materials. (b) Unit cell topology and geometric parameters.

thus compromising the reliability of the optimal design studies based on these models. Incidentally, similar discrepancies were observed in other 3D micro/nano-lattices with the polymeric preform manufactured by different techniques, such as projection microstereolithography [19], and two-photon lithography 3D direct laser writing (3D-DLW) [20,21]. In all these works, this large discrepancy is generally attributed to the complex stress state around the nodes (not predicted by simple models) and the presence of manufacturing-induced geometric imperfections. Note that due to the buckling-dominated nature of ultralight samples [16], the effects of defects can be even more significant in ultralight samples compared to denser counterparts. Wallach [22] performed a sensitivity analysis on 3D solid truss lattices, where imperfections were artificially introduced (by randomly removing bars from structure) to quantify their effect on stiffness and strength. However, to the best of our knowledge, no work has been performed to quantify the magnitude of defects naturally introduced by the manufacturing process in hollow lattices, and their specific effects on mechanical properties.

SEM imaging of hollow microlattice materials is useful to identify the sources of imperfection on these lattices (Fig. 1). Four classes of defects are evident: (1) geometric properties variations across the sample (Fig. 1a); (2) non-circular cross section of the bars (Fig. 1b); (3) geometric imperfections at nodes (Fig. 1c); and (4) cracks at nodes (Fig. 1c) or along and across the bars (Fig. 1d). The physical phenomena responsible for these defects are very process-specific and are explained in Section 2. In this work, we investigate the first two categories (imperfection in the bars) in great detail and investigate their effect on the mechanical properties of microlattices. The effect of nodal cracks is discussed elsewhere [23].

This paper is organized as follows: The manufacturing process is explained in detail in Section 2. Section 3 quantitatively presents the effects of geometric defects on the density of microlattice materials, and subsequently on their strength. Section 4 investigates the geometry of the defects at the individual strut level. In Section 5, Finite Element (FE) simulations and Nano-CT scan data are used to investigate the buckling strength of the imperfect bars extracted from a sample of hollow microlattice. In Section 6, a rigorous statistical analysis is performed on the imperfection data gathered from Nano-CT scanning of a number of hollow bars within the metallic microlattices to identify the dominant imperfection modes and build a stochastic field model that can be used to generate thousands of samples of imperfect bars. Through Monte Carlo sim-

ulations, the statistics of critical buckling load of the imperfect bars generated using the stochastic model developed in Section 6 is finally correlated with the strength scatter in a typical lattice sample in Section 7. The conclusions are summarized at the end.

## 2. Fabrication process and definition of geometric parameters

All nickel microlattice materials for this study are fabricated by HRL Laboratories (Malibu, CA), with the three-step process schematically illustrated in Fig. 2a: (i) a solid polymeric lattice is fabricated with the self-propagating photopolymer waveguide process (SPPW) [9,15,24]; (ii) the polymeric lattice is coated by a thin nickel film through electroless deposition; (iii) the polymeric lattice is removed using chemical etching techniques. This fabrication process, detailed in a number of references [7,9,12,25], is summarized here.

In the first step, the polymer microlattice templates are fabricated by shining parallel ultraviolet (UV) beams onto a vat of thio-lene liquid photomonomer through a patterned mask at different angles. When UV light reaches the thiol-ene liquid, it creates a periodic array of tubes with nodes that are located at the intersection of UV beams, hence forming an octahedral unitcell. This polymeric waveguide formation process happens in few seconds, making this technique significantly faster and more scalable than any competing technology. A wide range of architectures can be fabricated by changing the pattern of holes in the mask and the angle of the light rays relative to the mask. The polymeric lattices are then used as a template for depositing the structural film. Different materials can be deposited on the polymeric sample (e.g. nickel, copper, gold, etc.) [25], although this work focuses on nickel samples.

A standard, commercially available electroless kit (OM Group Inc. Cleveland, OH) is used to deposit a nickel-phosphorous alloy. The procedure consists of surface preparation by immersion in a potassium permanganate and sodium hydroxide solution, deposition of a catalyst (palladium) by immersion in an activator solution, etching in an accelerator solution, and finally nickel-phosphorus plating by immersion in a solution containing nickel sulfate, sodium hypophosphite, sodium malate and acetic acid. The plating bath is kept at pH 4.9 and 80 °C. The thickness of the film is dictated by the plating time: a 500 nm coating is produced in approximately 3 mins. Previous X-ray spectroscopy studies on the nickel film have

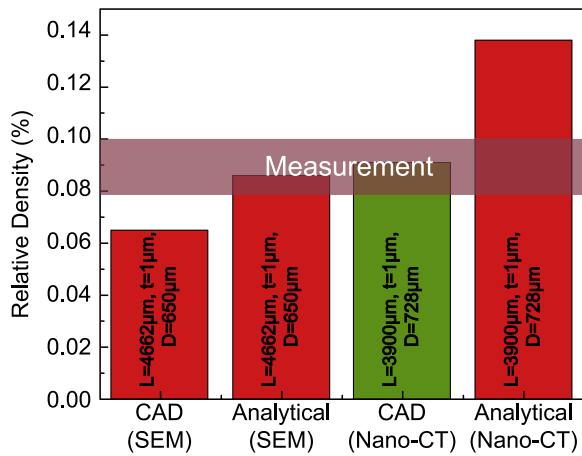


**Fig. 3.** Relative density calculations using analytical and CAD models; the dimensions are measured with Nano-CT scan and SEM imaging.

revealed that the film composition is 7% phosphorous and 93% nickel by weight and the TEM results have indicated a grain size of  $\sim 7$  nm. The materials are arranged as a supersaturated solid solution of phosphorous in a crystalline FCC nickel lattice with no  $\text{Ni}_3\text{P}$ . For more details on the process, refer to [9,12].

After coating of the wall material, the edges of the sample are sanded in order to expose the polymer substrate at each node. Finally, the polymeric template is etched out by using a chemical solution (3 M NaOH at  $60^\circ$ ) for 24 hrs, yielding a hollow microlattice sample. These samples can span up to three orders of magnitude in relative densities (0.01%–14%), depending on the choice of the geometric parameters (wall thickness, diameter, bar angles, etc.).

The process explained above is used to generate hollow lattices with the octahedral topology shown in Fig. 2b, with bars of length  $\ell$ , diameter  $D$ , wall thickness  $t$ , and truss angle  $\theta$ . The nickel layer manufactured with this technique has density of  $\rho = 8900 \text{ kg/m}^3$ , Young's modulus of  $E = 210 \text{ GPa}$ , Poisson ratio of  $\nu = 0.3$  and yield strength of  $\sigma_s = 2.5 \text{ GPa}$  (this high strength value is a result of the fine nano-scale grain size of the Ni-P material deposited with this process [9,12,16]).

A number of physical phenomena related to the SPPW process are responsible for the large majority of manufacturing defects present in these lattices (Fig. 1): (i) When the UV rays propagate through the monomer bath, a solid waveguide forms; however, although the mask hole is circular, instabilities in the propaga-

tion of the polymerization front result in the solidification of bars with longitudinal ridges (Fig. 1b); (ii) Small misalignment in the UV rays result in thickening of the nodes, as multiple bars no longer meet precisely at a point (Fig. 1a and c); (iii) The UV rays slightly diverge as they pass through the bath resulting in an increase in the diameter of the bars towards the bottom of the bath vat. Clearly, phenomena (ii) and (iii) become more problematic as the thickness of the sample increases; this effectively limits the number of unit cells in the vertical direction that can be manufactured in a single step with the SPPW process to  $\sim 2$ –5. To achieve the maximum number of layers, careful choices of intensity and exposure time are required. Note that all these defects are already present in the polymeric preform. Previous studies show that the thickness of the nickel coating is very uniform throughout the sample [9,12], consistently with the SEM measurements on the samples shown in this manuscript. The only class of defects that originate from the film itself is the presence of cracks at the nodes and along the bars (Fig. 1c and d), which are not explicitly accounted for in this work.

### 3. Analysis of geometric variability at the lattice level

The dimensions of the microlattice materials, i.e.: truss angle, length, wall thickness and bar diameter, are measured with a scanning electron microscope (SEM) with an accuracy of  $\pm 2^\circ$ ,  $\pm 3\%$ ,  $\pm 10\%$ , and  $\pm 15\%$ , respectively. During the measurements, significant variations in the diameter are observed. The geometric variations captured by SEM measurement on the hollow microlattices are investigated in more details in this section, and their effects on density and strength of lattice are studied.

A bulk microlattice sample with approximate dimensions of  $10 \text{ cm} \times 10 \text{ cm} \times 1.5 \text{ cm}$  containing of bars with  $D = 650 \mu\text{m}$ ,  $\ell = 4660 \mu\text{m}$ ,  $t = 1 \mu\text{m}$ , and  $\theta = 60^\circ$  (all based on SEM measurement) is used in our study. Note that the bar length is calculated by substituting the measured SEM diameter into the  $L/D$  ratio of the mask used in the fabrication process. The density of the lattices is measured at several scales: first the density of the whole sample is measured; subsequently, the sample is cut into four strips and the density of each strip is measured; finally, each strip is cut into three blocks and the density of each block was measured. The density of the 12 small blocks shows a standard deviation of  $\sim 5\%$  and maximum difference of  $\sim 15\%$ .

The relative density of the samples is calculated by inserting the lattice dimensions provided by SEM imaging into analytical and

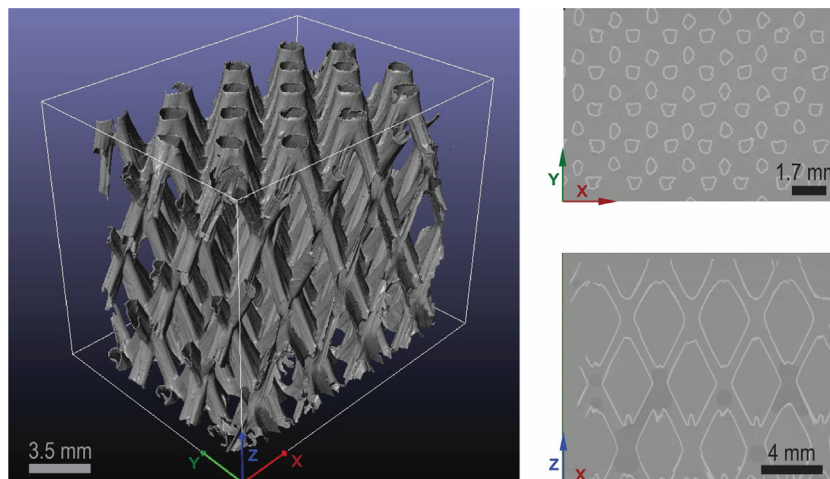


**Fig. 4.** Nano-CT image of a hollow microlattice material.

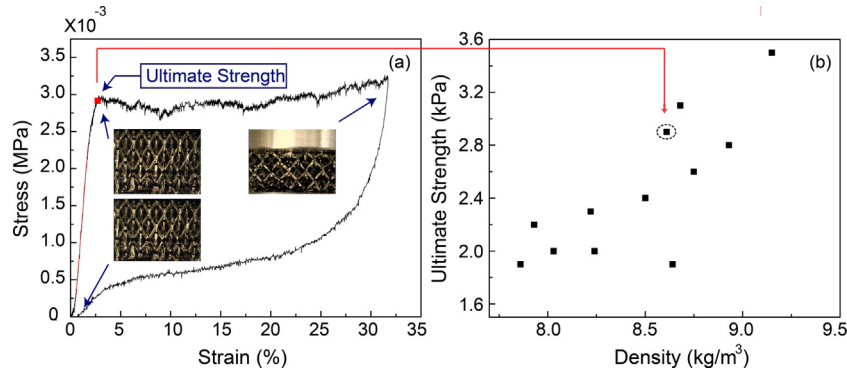


**Fig. 5.** (a) Representative stress-strain curve for a hollow microlattice in compression; (b) Maximum ultimate strength for the 12 different samples extracted from same bulk lattice coupon.

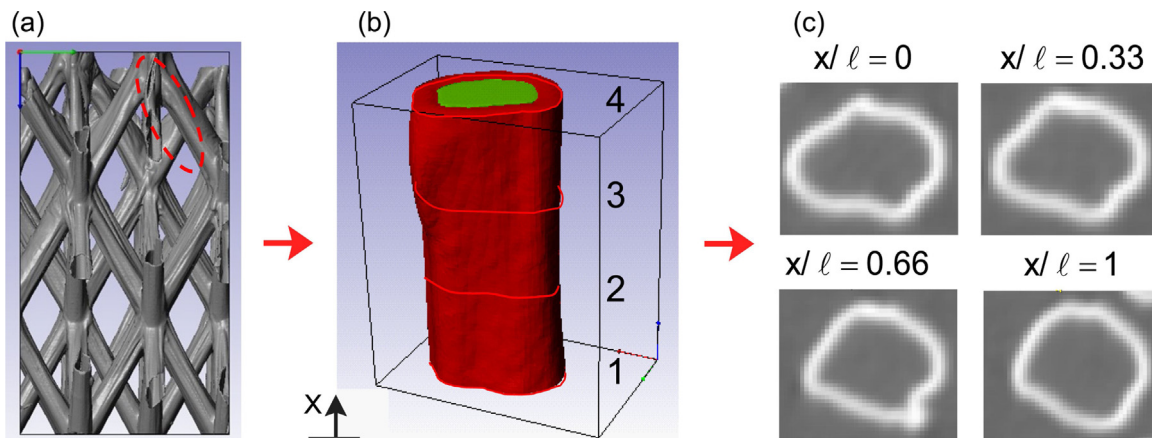


**Fig. 6.** (a) Nano-CT reconstruction of a microlattice material sample; (b) Nano-CT image of a single bar; (c) Cross sections of a representative bar at different locations along the bar, as obtained by Nano-CT characterization.

CAD models. The relative density can be approximated at first order in  $D/\ell$  and  $t/D$  as:

$$\bar{\rho} = \frac{2\pi}{\cos^2\theta \sin\theta} \left(\frac{D}{\ell}\right)^2 \frac{t}{D} \quad (1)$$

with all the geometric parameters defined in Fig. 2b. This model neglects any mass clipping at the nodes and hence significantly overestimates the relative density for lattices with stubby members ( $\ell/D < 10$ ), even if extremely lightweight [18]. Conversely, in the CAD model (see Fig. 2b), the surface area of a unit cell (with idealized geometry expressed by the mesh generator described in [16,18]) is multiplied by the film thickness (assumed to be  $1 \mu\text{m}$  uniformly across) and divided by the cell volume to calculate the density. As shown in Fig. 3, both of these models underpredict the relative density of the lattice (the CAD model by as much as 30%). This can be explained by: (1) material accumulation on the edges of the specimen, (2) non-circular cross sections, and (3) inaccuracy in measuring the dimensions using SEM.

To better understand this discrepancy, one sample is imaged by means of Nano Computed Tomography (Nano-CT) using a Xradia VersaXRM<sup>TM</sup> 410 scanner (see Fig. 4). As the resolution of this instrument ( $\sim 25 \mu\text{m}$ ) is significantly larger than the wall thickness ( $\sim 1 \mu\text{m}$ ), the wall thickness can not be captured. Given that electroless deposition is a very conformal process, we will assume that the wall thickness value of  $\sim 1 \mu\text{m}$ , measured locally by SEM, is uniform throughout the sample. Conversely, the diameter and the length of the bars can be measured accurately, and so can the geometric defects associated with these quantities.

Approximately, 150 bar are extracted from the raw CT data using the SIMPWARE software version 7.0 and the average diameter ( $D \sim 728 \mu\text{m}$ ) and length ( $\ell \sim 3900 \mu\text{m}$ ) are obtained. These values differ from those obtained by SEM measurements on the same sample (diameter of  $650 \mu\text{m}$  and length of  $4662 \mu\text{m}$ ). The variation in the diameter measurement is attributed to spatial variations of the diameter through the sample; and non-circularity of the bars. The variations in length are associated to slight misalignment in the UV rays which causes dislocation of the nodes from their intended positions, thus resulting in length variations from bar to bar.

The relative density of the lattice is recalculated from the Nano-CT measured length and diameter (assuming a uniform thickness measured by SEM), using both the analytical and the CAD models. The results presented in Fig. 3 show that the CAD model with Nano-CT measurements captures the measured density accurately, while the first-order analytical model, not surprisingly, overpredicts the density. These results also indicate that accurate dimensions, representative of the entire sample, cannot be easily extracted by a few local SEM measurements. Finally, notice that the good agreement in density between measurements and models that assume uniform wall thickness confirms the validity of this assumption.

To further investigate the effects of these dimensional variations on the properties of the microlattice materials, the strength of all the 12 samples used above are measured by uniaxial quasi-static compression tests. All tests are conducted with a servo electric INSTRON 8862 frame, equipped with a 250 lb Honeywell load cell and a National Instrument SCXI data acquisition system. A constant displacement rate of  $0.1 \text{ mm/s}$  is used for all tests. A representative engineering stress-strain curve is depicted in Fig. 5a. Note

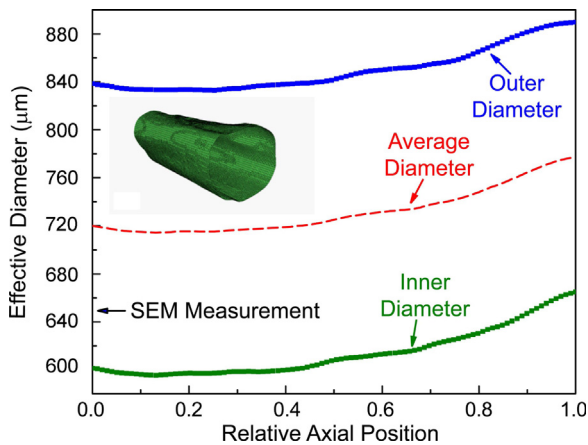


**Fig. 7.** Inner, outer and average diameter of a single bar extracted from a Nano-CT reconstruction (the inset shows the mesh of a single bar extracted from Nano-CT images).

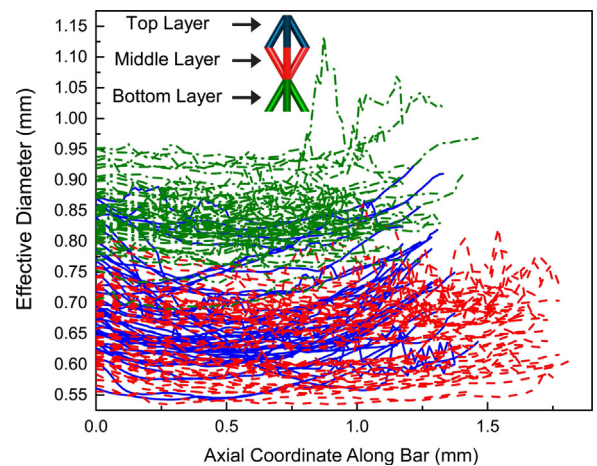
that these samples show full recoverability under 30% strain (samples with ultra-low relative densities show full elastic recovery up to  $\sim 50\%$  compressive strain [12,13]). This recoverability is due to the extremely low thickness-to-diameter ratio in the bars and the very high yield strength of the nickel alloy. Combined, these effects ensure that the bars deform by local buckling near the nodes; after the bar diameters are pinched and locally reduced to a line, large rotations of the bars with very low (and purely elastic) strain in the material enable the massive strains observed at the macroscale. This unique failure mechanism has been discussed in detail in [9,12,16,25]. Clearly, increasing the wall thickness beyond a critical value results in a switch from buckling to yielding-dominated response, and the macroscopic recoverability is lost. This transition occurs at relative densities much higher than those discussed in this paper [13,25]. The conclusion is that local elastic buckling is the strength-limiting phenomenon in all the lattices studied herein.

Fig. 5b shows the maximum ultimate strength vs the density of the 12 lattice samples extracted from the same test coupon. The results indicate that the strength of the samples correlates fairly well with the density; however, a significant scatter (as high as a factor of 2) is observed, which cannot be explained by density variation in the bulk sample. To further explore the effect of the geometric imperfections on the strength of the microlattices, the geometric defects in the individual bars are studied in detail in the next section.

#### 4. Analysis of geometric defects at the individual strut level

As the images captured by SEM (Fig. 1) and Nano-CT (Fig. 4) show, the geometry of individual bars, in the hollow microlattice, varies from bar to bar; moreover, the cross sections of the bars are markedly non-circular. An investigation of individual bars extracted from the Nano-CT reconstruction (Fig. 6a) shows clear variation in cross-section geometry along the bar (Fig. 6b and c). Therefore, a detailed study is needed to understand the geometric imperfections of the bars in the lattice. In this section we quantify such geometric defects.

All the bars ( $\sim 150$  bar) are aligned and perfectly cut in order to have a flat surface at both edges (Fig. 6b). A shell mesh of every single bar is extracted from the Nano-CT data by using the SIMPLEWARE software (inset in Fig. 7). Note that since the minimum feature resolution of the Nano-CT ( $\sim 25 \mu\text{m}$ ) is much larger than the bar thickness ( $\sim 1 \mu\text{m}$ ), the CT scan shows an artificially thicker wall (red edge in Fig. 6b). Therefore, two different shell mesh mod-



**Fig. 8.** The average diameter of the bars within different layers in the lattice.

els are extracted from Nano-CT bars: (1) outer layer mesh (2) inner layer mesh (Fig. 6b).

A custom geometry processor is written to analyze the hollow bar meshes extracted from the Nano-CT data and measure the diameter accurately. This system divides each individual bar into several sections  $5 \mu\text{m}$  apart along the x axis (orthogonal to the plane of the cross section) and calculates the perimeter of each cross section to extract the nominal diameters. Fig. 7 shows the effective diameter (perimeter divided by  $\pi$ ) of the inner and outer layer at different cross sections for a single bar. To calculate the effective diameter of each bar we average the inner and outer diameters (shown as a dashed line in Fig. 7).

In order to decrease the computational cost, a scan with  $50 \mu\text{m}$  resolution is also performed. The maximum difference observed between the scans with  $25$  and  $50 \mu\text{m}$  resolution is only  $\sim 4\%$  and no difference is seen in the cross-sectional geometry; therefore, low resolution data is adopted for all the analyses. Note that, due to the artificial thickness of the bars, neither of the two different shell meshes extracted from the Nano-CT data (outer and inner shell, as explained above) in actuality represents the real bar, which is somewhere in the middle of these two models. The actual middle shell is extracted using the SIMPLEWARE software, and analyzed again, to measure the diameter at different cross sections. The results indicate that the average diameter (captured from average of the inner and outer shell model) is very close to the middle shell data (less than  $\sim 1\%$  error). Therefore, for future analyses, the middle shell model is used instead of two inner and outer shells.

The middle shell data of the bars extracted from Nano-CT measurements are used to calculate the bar diameter at different locations. Fig. 8 shows the diameter as a function of the location along the bar, for all bars within the lattice block. The results indicate that the diameters of the bars at the bottom layer tend to be bigger than the diameters of the ones in the middle and top layers of the lattice. This is mostly due to a divergence of the UV rays as they pass through the monomer bath: as the UV rays diverge, the diameter of the bars increase.

In order to quantify the variation of the bars from a perfect cylinder, the following method is used. First of all, the average bar diameter for the whole lattice is calculated (the average diameter of a bar is defined as the diameter of a circular bar with the same surface area as the imperfect bar). Subsequently, the coordinate of the centroid of each cross section along each bar is extracted, and the average centroid location for each bar is calculated. At each cross section along the bar length, a circle is drawn with diameter equal to the average diameter in the lattice and center located at the average centroid of that bar. The difference between the local

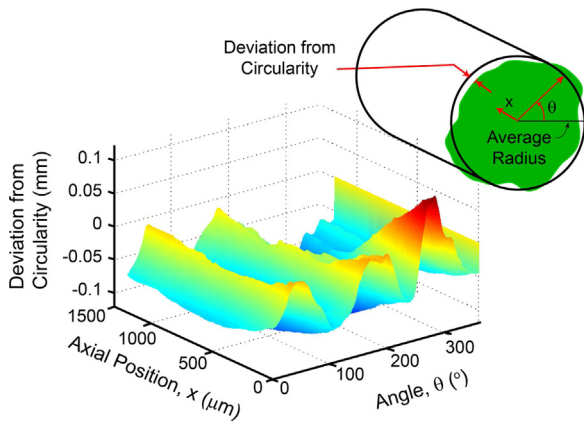


**Fig. 9.** Deviation of bar cross section from circularity as a function of angular and axial coordinates for a representative bar.

radius of the CT reconstructed bar and the radius of the average circular bar (denoted as ‘deviation from circularity’ in the inset in Fig. 9) is extracted as a function of the angular and axial coordinates of each bar (see inset in Fig. 9 for coordinates definition) in  $1^\circ$  and  $5 \mu\text{m}$  increments, respectively.

As Fig. 9 shows, large deviations from circularity are observed at some longitudinal locations and angles. In the next section the role that these geometric imperfections play in altering the strength of these bars is studied in detail.

## 5. Effect of bar shape on buckling strength

To quantify the effects of non-circularity on the strength of microlattices, the bars derived from Nano-CT scan are modeled by finite elements (FE) analysis (using the commercial software ABAQUS), and the buckling loads are extracted. A single bar in a microlattice under uniaxial macroscopic compression experiences a combination of shear and axial loads and a bending moment. As the actual bar is non-circular, the angle at which the shear load is applied affects the critical load; therefore, the shear component of the load is scanned around the bar to test all possible orientations of the bar relative to the loading direction (Fig. 10a).

Shell elements (S3) are used to model the bars with  $1 \mu\text{m}$  thickness. The individual hollow bars are loaded with an inclined force, to capture the combination of axial and shear load. One edge of the bar is fully clamped while the other edge is allowed to translate in all directions (albeit as a rigid body) but not rotate. Nickel is model as elastic material with the material properties given in Section 2. To capture the effects of geometric nonlinearity, the bar is preloaded statically prior to the buckling analysis. The shear load is applied in 20 different directions around the circle ( $18^\circ$  apart as depicted in Fig. 10a), resulting in 20 FE simulations per bar and a total of  $\sim 3000$  simulations. In order to prepare the input deck for FE simulation as well as extract buckling loads, a Python script is developed. All simulations are run on the UCI’s HPC cluster.

The buckling load of a representative CT-derived bar is depicted in Fig. 10b. The results show the critical buckling loads at different orientations of the bar relative to the loading direction, along with their mode shapes. It is clear that, as mentioned above, the critical buckling load is strongly affected by the orientations of the bar in the unit cell. This particular bar could fail by local buckling in either shear or compression, depending on their orientations in the unit cell. Note that, according to buckling modes depicted in Fig. 10b, the critical load for shear buckling is often higher than that of compression buckling.

The critical buckling load calculated for the CT-derived bar is compared to the analytical model and FE simulation results

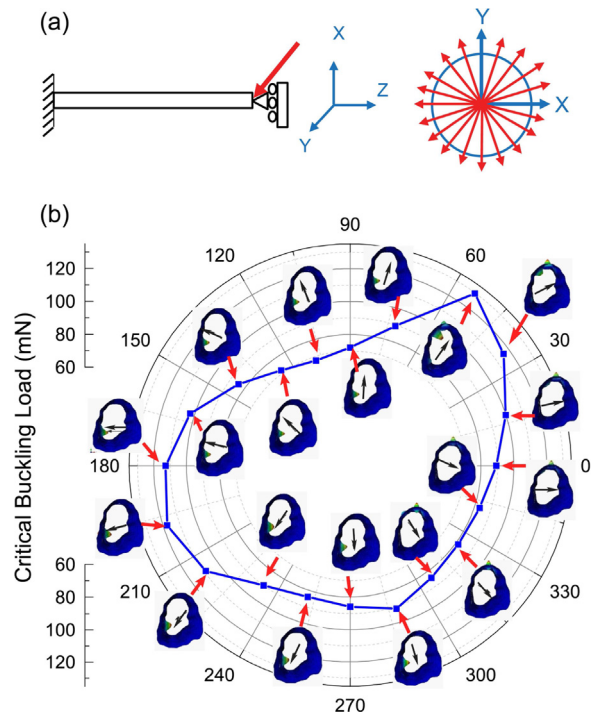


**Fig. 10.** (a) Schematic view of one bar in the unit cell under a combination of compression and shear. (b) The critical buckling loads of a CT-derived bar and their buckling mode shapes.

obtained for a perfect bar to better understand the effects of non-circularity. Previous studies (see [16]) on failure mechanism of hollow microlattice materials show that in the ultralight regime the bars fail under local buckling. Buckling may occur by shell shear (due to the shear load on the bar), in which case it is generally distributed along the full length of the bar, or by shell compression due to bending moment and axial load on the bar, in which case it is highly localized near the nodes where the normal compressive stress is maximum. For slender bars, compression buckling is generally the dominant failure mechanism, whereas shear buckling governs the strength of stockier bars.

The bar will buckle by shell compression when the maximum compressive stress in the bar in the unit cell equals the critical local buckling stress [26]. The buckling load of a perfectly circular bar in the unit cell under compression-bending can be expressed as [13]:

$$P_{cr,bar}^{b+c} = \frac{P_{cr}^{b+c}}{4} = \frac{2\pi Et^2}{\sqrt{3(1-\nu^2)(\sin\theta + \frac{2\ell\cos\theta}{D})}} \quad (2)$$

When the maximum shear stress in the bar wall reaches the critical shear stress [27], shear buckling initiates; this condition can be expressed as [13]:

$$P_{cr,bar}^{sh} = \frac{P_{cr}^{sh}}{4} = \frac{3\pi Et^2}{2\cos\theta} \sqrt{\frac{Dt/2}{\ell}} \quad (3)$$

A perfectly circular bar with the same length and perimeter as the actual bar depicted in Fig. 10b (length of  $\ell = 1.28 \text{ mm}$  and average diameter of  $D = 708 \mu\text{m}$ ) would fail by shear buckling (Fig. 11a). Importantly, the results depicted in Fig. 11a show that the critical buckling load of an actual bar is always lower than for a circular bar with the same perimeter (and hence weight), irrespective of the loading direction. Hence deviations from circularity always have a detrimental effect on the specific strength of hollow lattices.

Visual inspection of various cross sections of the bars in microlattice materials suggests that the cross sections are at times elliptical rather than circular. Therefore, it is constructive to com-

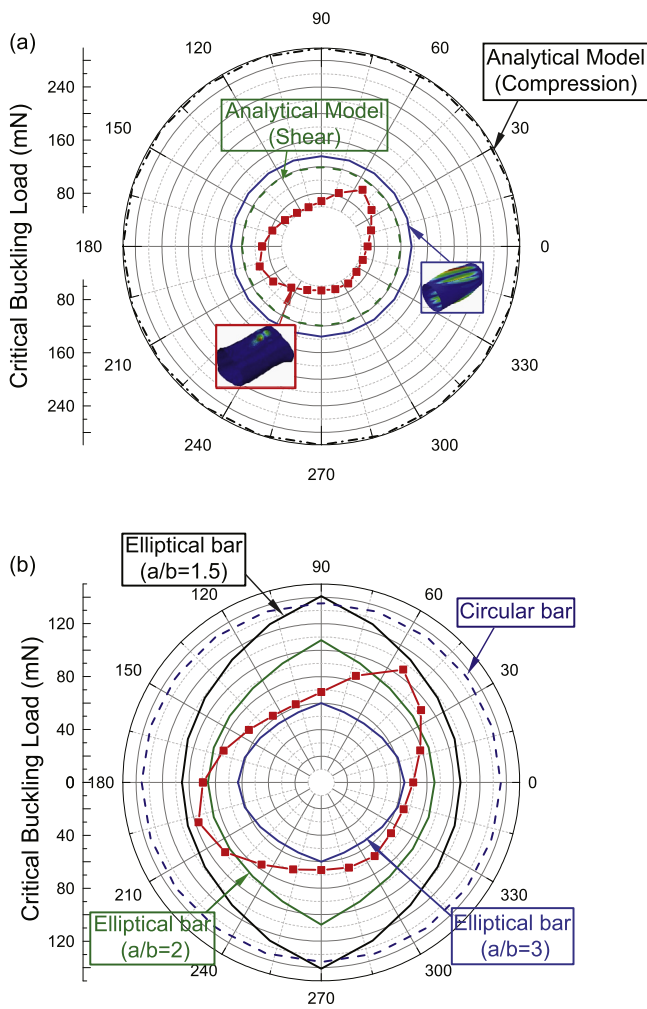


**Fig. 11.** (a) The comparison of the critical buckling load of a CT-derived bar, and a perfectly circular bar with the same perimeter (and hence weight); analytical model and FE simulations (b) The Comparison of the critical buckling load of a CT-derived bar, and bars with ideal circular and elliptical geometries.

pare the behavior of the CT-derived bar with elliptical bars of the same perimeter. For the purpose of this comparison, three elliptical bars with aspect ratios of  $a/b=1.5$ ,  $a/b=2$ , and  $a/b=3$  are used. Fig. 11b compares the critical buckling load of the CT-derived bar, and perfectly circular and elliptical bars of the same perimeter, loaded at different angles. Surprisingly, the results indicate that bars with elliptical cross sections are nearly always weaker than the perfectly circular bars, irrespective of the loading direction. Moreover, the critical buckling load of the CT-derived bar is close to that of a perfect bar with an elliptical cross section and aspect ratio of  $a/b=2$ . This finding could be useful for analytical studies of lattice strength that incorporate the effect of defects.

Note that actual bars in a microlattice are almost always longer than the CT-derived bar depicted in Fig. 10 and Fig. 11, as clipping must occur sufficiently far away from the nodes. Therefore, to confirm that the same conclusions hold for longer bars, the circular and elliptical bars are modeled with a 3.9 mm length (the average length of the bar in the unit cell). The results confirm that bars with elliptical cross sections are weaker than the ones with circular cross section. In addition, by increasing the length, the difference between the critical buckling load of bars with circular and elliptical cross sections is increased.

The critical buckling load results of a single CT-derived bar were presented in this section as a representative behavior of all the bars

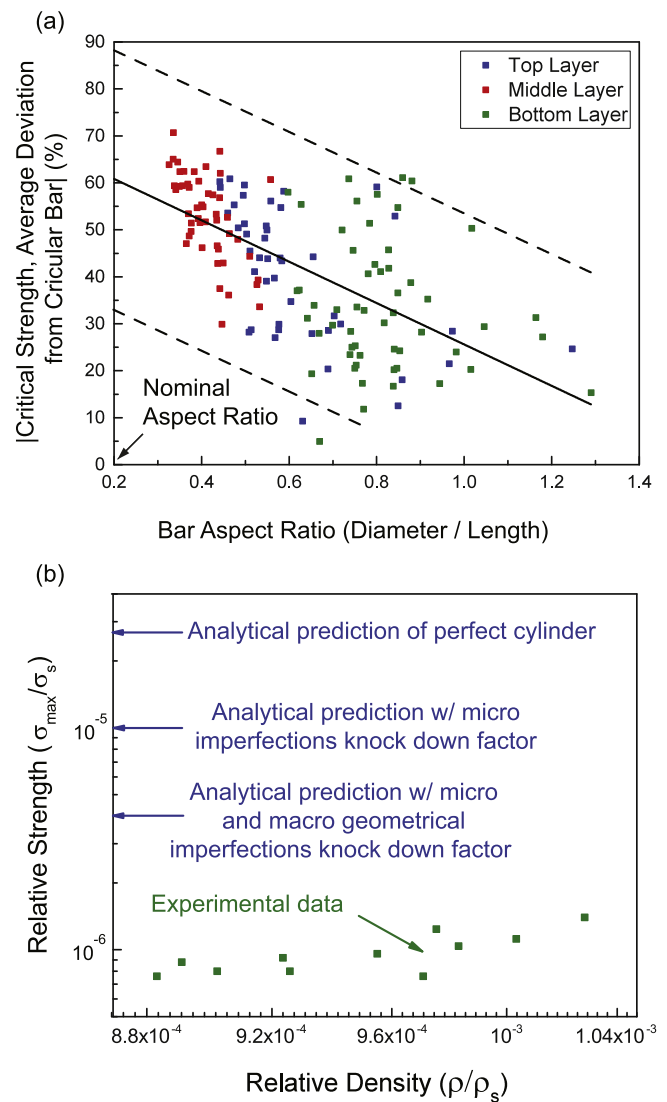


**Fig. 12.** (a) Average deviation of the critical load of CT-derived bars from circular bar versus bar aspect ratio (color coded based on layer). (b) The comparison of experimental data and analytical predictions of the strength of a bulk lattice calculated based on local buckling with and without accounting for micro and macro geometric imperfections.

in the microlattice. However, the behaviors of all the bars are important for predicting the performance of the lattice. Therefore, all the CT-derived bars are modeled and their critical buckling loads are calculated. The result for each bar is compared to the critical load of a circular bar with the same surface area. The average deviation (over circumferential angles) of the critical buckling load for the CT-derived bar from the perfectly circular bar is calculated for all the bars. Fig. 12a shows this deviation versus the aspect ratio of the extracted bar segments. Two observations can be made: (i) Segments extracted from the bars in the middle of the sample are significantly more slender than segments extracted from either the top or bottom layers. This can be explained by observing that bars at the top or bottom layers share one node that was in contact with the sides of the vat during polymerization; these terminal nodes tend to be thicker (See Fig. 6a). As it is difficult to cut bars close to the nodes from a CT-reconstruction of the sample, these extracted bar segments result in stockier bars than those in the middle layer. (ii) By decreasing the aspect ratio, the deviation of the critical load of the CT-derived bars from the circular bar is increasing.

It is important to emphasize once again that the aspect ratio of the bar segments depicted in Fig. 12a is different from the actual aspect ratio of the bars (which merge seamlessly into the nodes in the actual samples). Noting that the nominal aspect ratio of the bars in this lattice is about 0.2 (with average diameter of 728  $\mu\text{m}$  and average length of 3900  $\mu\text{m}$ ), the deviation of the critical load of CT-derived bars from circular bar is expected to be around 60% (see solid line in Fig. 12a).

The buckling strength of the microlattice can be expressed as  $\sigma_{\text{lb}} = p_{\text{cr}} / (2\ell^2 \cos^2 \theta)$  where  $p_{\text{cr}}$  is the critical buckling load of the unit cell (calculated from Eq. (2) or Eq. (3)) and  $2\ell^2 \cos^2 \theta$  is the effective area of the unit cell. The relative strength (buckling strength of the lattice over the yield strength of nickel,  $\sigma_s = 2.5 \text{ GPa}$ ) versus the relative density, plotted in Fig. 12b, indicates that the analytical prediction for strength of the lattice is roughly 25 times higher than what is observed in experiments. In practice, the load carrying capacity of hollow thin wall cylinders are always lower than predicted by elastic buckling theory, as very small deviations in the shape of cylindrical shells (henceforth referred to as *micro-imperfections*) have a strong effect on the critical buckling load – with the effect increasing with decreasing wall thickness. This discrepancy was carefully studied experimentally in the 1960's [28], and was quantified by a knock-down factor on the buckling load. This leads to a modification of Eq. (2) in the following form [13,28]:

$$p_{\text{cr,bar}}^{b+c} = \frac{p_{\text{cr}}^{b+c}}{4} = \frac{2\gamma\pi Et^2}{\sqrt{3(1-\nu^2)(\sin\theta + \frac{2\ell \cos\theta}{D})}} \quad (4)$$

where the knock down factor reads (see [28]):

$$\gamma = 1 - 0.901(1 - e^{-\phi}) \quad (5)$$

with:

$$\phi = \frac{1}{16} \sqrt{\frac{D}{2t}} \quad (6)$$

Using Eq. (4), the analytical buckling strength of the lattice is decreased by factor of about 2.5 times (from about  $2.5 \times 10^{-5}$  to  $10^{-5}$ ). However, our extensive FE analysis of CT-derived hollow bars in the microlattice (see Fig. 12a) indicated that the deviation of critical load from perfect cylinder for a bar with aspect ratio of about 0.2 could be as high as 60%. This deviation, due to the macroscopic manufacturing imperfections depicted in Fig. 1 (henceforth referred to as *macro-imperfections*), if considered in the form of an additional knockdown factor, brings down the prediction by the analytical model (see Fig. 12b) to a value that is closer to the experimental data. Even after all these considerations, though, a 4X discrepancy between analytical predictions and average experimental results still remains, which is tentatively attributed to two factors: (i) imperfections at the nodes, where most local buckling events initiate, and (ii) presence of cracks along the bars or at the nodes (see Fig. 1). A finite elements analysis of the nodes would in principle allow us to quantify the effect of nodal shape on buckling strength of the lattice. Unfortunately, extracting meaningful information from such analysis is extremely difficult. On the other hand modeling single unit cells extracted from CT data provides results that are dramatically affected by the clipping location. Given these challenges, we have not attempted to explicitly model the effect of the nodal geometry on lattice strength; nonetheless, the bars have been clipped as close as possible to the nodes, allowing us to capture some of the nodal geometry effect in our bar buckling strength calculations. As for the effect of nodal cracks on the lattice strength, this is a complicated fracture mechanics problem that will be addressed in a separate publication [23].

Regardless of the disagreement between analytical predictions and average experimental measurements, the high scatter observed in FE analysis results for the buckling strength of CT-

derived bars and its correlation with experimental data (Fig. 12) still needs further justification. In the next section a rigorous statistical characterization of imperfections in Nano-CT derived bars and their effect on the strength is presented to provide such justification.

## 6. Statistical characterization of geometric imperfections

One of the most common ways to represent (stochastic) variabilities (either in material properties or the geometry) is through the use of stochastic processes (or fields) that are numerically constructed to encapsulate the information extracted from data such as the empirical correlation structure or the marginal probability densities [29–31]. As the data available is often limited, the path taken towards any probabilistic construction must ensure the consistency; that is, as more data is gathered the more closely the statistical properties of the constructed stochastic process should resemble those of the underlying process. In what follows we perform a statistical analysis of geometric imperfection data gathered from Nano-CT scanning of a number of bars within the metallic microlattices with two goals: (i) identifying the dominant imperfection modes, and (ii) building a stochastic field “model” that can be used to generate samples of imperfect bars. While the first of these two goals is more of an exploratory nature, the second one would allow for a statistical analysis of a particular mechanical response of bars, e.g. buckling capacity; an analysis that could be used to shed light on how nonlinear behavior of stability-critical structures is affected by geometric variabilities characterized by real data [32–34].

## 7. Stochastic field model development

The idea we follow here is based on an orthogonal functions expansion scheme, Karhunen-Loeve (or KL) transform [35], that allows for writing a stochastic process in terms of a series representation that involves a set of uncorrelated random variables and a set of “deterministic” functions. No particular form for the statistics, e.g. correlation structure or marginal probability distribution of the stochastic process, is assumed. Instead the mean, correlation function, and the marginal (and potentially the joint) distributions of the reconstructed field are matched with those of the measurements. To further explain the idea here let  $g(x, y, \omega)$  be the stochastic field representing the geometric flaws. Here,  $x$  and  $y$  represent spatial dimensions and  $\omega$  represents the stochastic dimension, that is any  $\omega = \omega_0$  corresponds to a realization (or a sample) of the stochastic process. Using KL transform this stochastic field can be written in the form of following series representation:

$$g(x, y, \omega) = \bar{g}(x, y) + \sum_m \sqrt{\lambda_m} \phi_m(x, y) \zeta_m(\omega) \quad (7)$$

In the above equation  $\bar{g}(x, y)$  denotes the mean (average) geometric flaw field,  $(\lambda_m, \phi_m)$  denote the eigenvalue and eigenvector of an eigenvalue problem involving the covariance kernel of the process, and stochastic quantities  $(g(x, y, \omega)$  and  $\zeta_m(\omega))$  are identified by their dependence on  $\omega$ . The real connection between Eq. (7) and the gathered data on geometric imperfections is that in practice we deal with samples of a discretized version of the continuous stochastic process, that is samples of a random vector. The above equation is therefore re-written in the following form:

$$G(\omega) = \bar{G} + \sum_m \sqrt{\alpha_m} \Phi_m \xi_m(\omega) \quad (8)$$

where the characters  $G$ ,  $\bar{G}$  and  $\Phi_m$  now denote vectors. Furthermore, the eigenpairs  $(\alpha_m, \Phi_m)$  of the covariance matrix of  $G(\omega)$  are approximated using the eigenpairs of the sample covariance matrix for geometric imperfection data. Eq. (8) is also referred to as

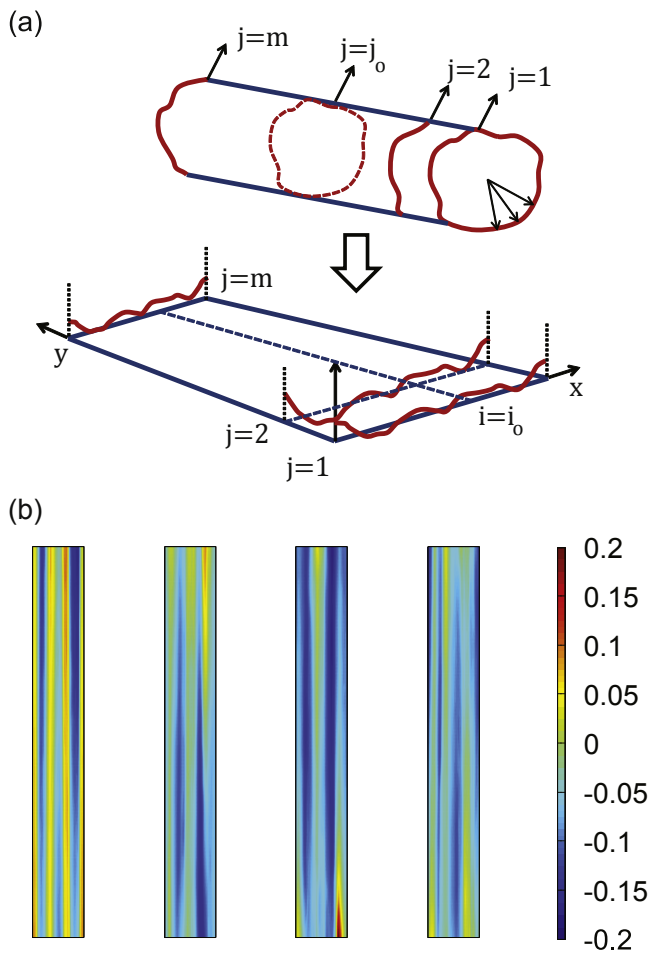


**Fig. 13.** Transforming 3D geometric imperfections onto 2D data sets: (a) Projection of an imperfect hollow bar to a 2D imperfection map; (b) 2D imperfection maps for 4 representative bars: the vertical axis represents the longitudinal coordinate along the bar, while the horizontal axis shows the circumferential coordinate; the contours denote the imperfection amplitude.

a Proper Orthogonal Decomposition (POD), since the eigenvectors  $\Phi_m$  are orthogonal. It allows for transforming the high dimensional vector  $G$  to a few “dominant” eigenmodes and a few “uncorrelated” random variables  $\xi_m$ , since most of the eigenvalues  $\alpha_m$  (except the first few) are close to zero. Realizations (or samples) of the geometric imperfection field gathered for example from Nano-CT imaging of the imperfect bars within the lattice are then projected onto the set of  $\Phi_m$ s to obtain samples of  $\xi_m$ s. Once samples of  $\xi_m$ s are available, statistical estimation methods can be used to estimate their probability density which can then be used to generate more samples  $\{\hat{\xi}_{mn}\}_{n=1}^N$  (with  $N$  the size of sample) using a standard stochastic simulation technique. Linear combinations of the dominant eigenmodes with coefficients taken from these new samples then constitute “new” realizations of the geometric imperfection field which can then be used for further analysis.

### 8. Practical implementation on nano-CT data

Fig. 13a shows how a sample from geometric imperfection field measured along the length of a typical hollow bar and at different angular positions is turned into a 2D sample. Assuming the imperfection measurements are recorded at discrete points on the surface (say  $(i, j) = (i_0, j_0)$ ), a typical sample is stored in a matrix resembling a digitized version of an image (see Fig. 13b). A sample of the ran-

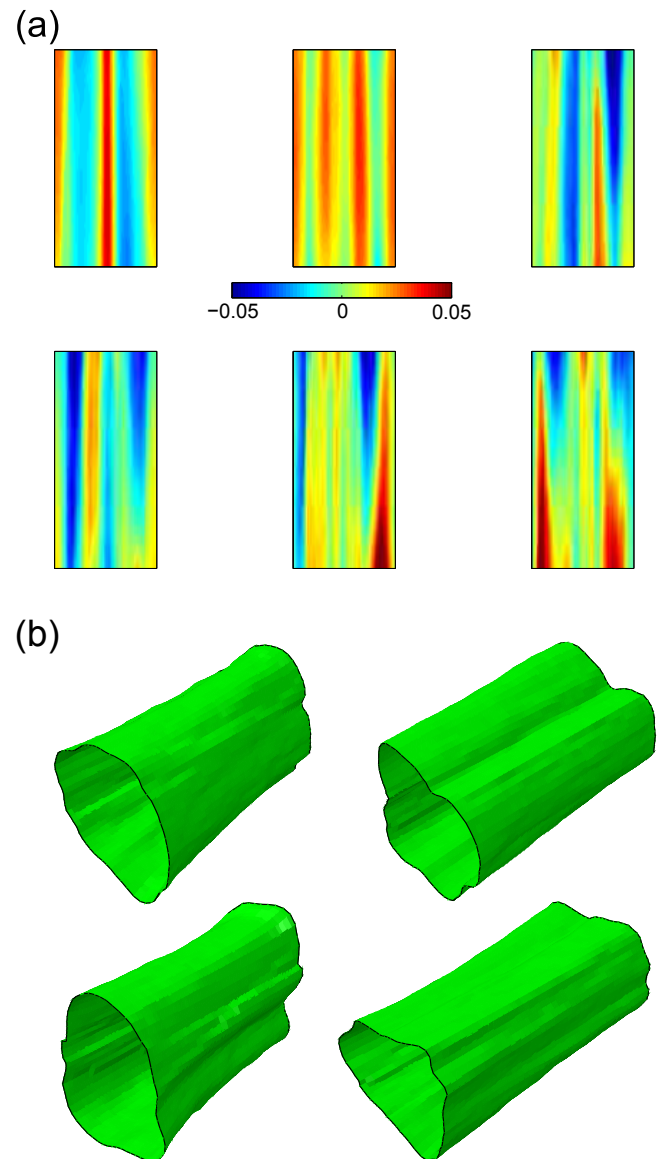


**Fig. 14.** The dominant imperfection eigenmodes and artificially generated imperfect hollow bars:(a) the first 6 dominant imperfection modes; (b) four imperfect hollow bars generated using the stochastic model.

dom vector  $G$  in the above discussion is the vector obtained by concatenating the columns (or rows) of such a matrix. Once samples of  $G$  are available, one would proceed to identifying the first few dominant eigenmodes, transformation of samples of geometric imperfections to realizations of uncorrelated random variables  $\xi_m$ s in the above discussion and finally the construction of stochastic field from which more samples of the geometric imperfections can be generated. Fig. 14a, for example, shows the first few dominant imperfection modes obtained from POD analysis of hollow bar imperfection data gathered in this study while Fig. 14b shows four imperfect hollow bar realizations generated by using these dominant modes in Eq. (8) and sampling from random variables  $\xi_m$ s.

### 9. Correlating imperfection statistics to scatter in buckling strength

To further investigate the origin of scatter observed in FE analysis of CT-derived bars and its correlation with experimental data, a large number of (about 120) hollow bars form within the sample

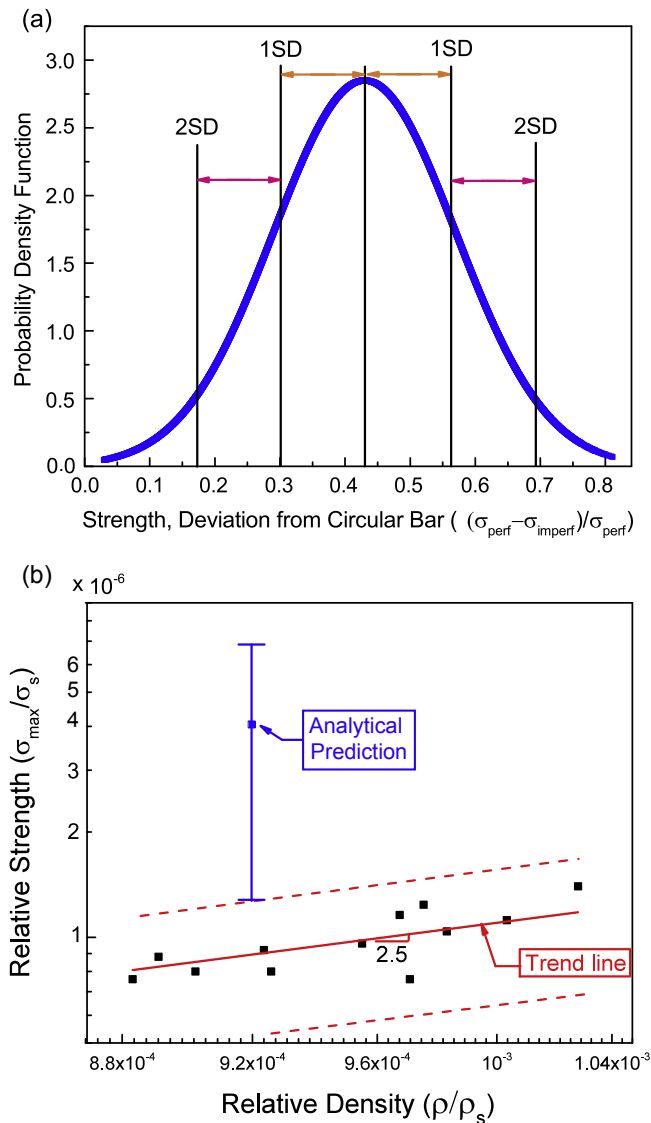


**Fig. 15.** (a) Frequency of percent deviation of critical strength of imperfect bars from that of the perfect bar. (b) The 95% confidence interval upper and lower bounds for the strength of a bulk lattice calculated based on buckling strength of non-circular bars both analytically and experimentally.

lattice is imaged by Nano-CT scanning. The geometric imperfections extracted from these bars (see Section 3) are used to build a stochastic model of geometric imperfection field (see Section 5) which is then used to generate 2000 imperfect bars. Note that since the CT-derived bars are detached from the nodes, it is impossible to extract bars with the actual length of 3.9 mm. However, the analysis of the effect of stochastic deviations from circularity on the “extent” of scatter in FE simulations and the deviation from experimental results for one particular bar length can be extended to other bar lengths. Finite element buckling analysis is performed on the imperfect bars generated using the stochastic model under the same conditions as those described in Section 4. The shear load is applied along 20 different angles around the circle ( $18^\circ$  apart; see Fig. 10), resulting in 20 FE simulations per bar and a total of 40,000 simulations.

The critical buckling strengths captured from these simulations are compared to the critical buckling strength of a perfect cylinder with the average diameter of lattice, and the percent deviations are calculated. Fig. 15a shows the Gaussian equivalent frequency of percent deviation of the critical buckling strength of gener-

ated imperfect bars from that of a perfect bar. The result shows a standard deviation of about  $\sim 14\%$  and a 95% confidence interval corresponding to  $43 \pm 28\%$ . The dashed green lines in Fig. 12a in Section 4 above and below the trend line (solid green line) now represent the extent of scatter expected. It can be seen that these lines now comfortably “hug” the data indicating the validity of our stochastic analysis.

Fig. 15b now shows the analytical prediction of strength of the lattice taking into account the micro and macro geometric imperfection knock down factors (see Section 4) along with the confidence interval deduced from stochastic analysis of macro geometric imperfections presented above. The solid red line in this figure shows a 2.5–1 trend line for relative strength versus relative density variation observed in previous studies (see [12]), while the dashed red lines depict the upper and lower confidence interval bounds. It is seen from this figure how judiciously guided adjustments (based on data-driven stochastic analysis) have the potential to bridge the gap between analytical and numerical predictions and experimental measurements. It is, however, noted that due to stability-critical and flaw-sensitive nature of the mechanics of ultralight hollow microlattices, the analysis presented here, only covers a subset of reasons underlying such gaps and is not exhaustive.

## 10. Conclusions

In this work, the effects of manufacturing defects on the strength of ultralight hollow microlattice materials produced by SPPW templating are investigated. The density and strength variations measured across a bulk sample show that strength correlates quite well with density, albeit with a significant scatter. Nano-CT scans are performed to accurately measure the dimensions of each bar in the sample, to identify the source of imperfections and quantify the effects of these imperfections on the strength of the lattice. Aided by a rigorous stochastic analysis, this study indicates that the significant non-circularity of the bars is largely responsible for the scatter in experimental strength data. This suggests that by controlling the manufacturing process of the lattice and by decreasing the bar non-circularity we can obtain lattices with much better mechanical performance. Although the quantitative results in this work are specific to microlattices fabricated by SPPW templating, the methodology presented herein is equally applicable to lattices (and in fact any architected materials) produced by other manufacturing approaches, in particular additive processes, such as Fused Deposition Modeling, Stereolithography and Selective Laser Sintering.

## Acknowledgments

The authors are indebted to Tobias Schaedler, Alan J. Jacobsen and William B. Carter of HRL Laboratories for providing samples and for useful discussions. This work was financially supported by NSF under Awards # CCM1-1401496, CMMI-1235235, and CMMI-1351742. The Abaqus® Finite Element Analysis software is licensed from Dassault Systemes SIMULIA, as part of a Strategic Academic Customer Program between UC Irvine and SIMULIA. The authors are thankful to UCI High Performance Computing Cluster team (HPC) for their support.

## References

- [1] M.F. Gibson, *Cellular Solids: Structure and Properties*, Cambridge University Press, 1999.
- [2] A.G. Evans, J.W. Hutchinson, M.F. Ashby, Multifunctionality of cellular metal systems, *Prog. Mater. Sci.* 43 (1998) 171–221.

- [3] H.N.G. Wadley, N.A. Fleck, A.G. Evans, Fabrication and structural performance of periodic cellular metal sandwich structures, *Porous Mater.* 63 (2003) 2331–2343.
- [4] A.G. Evans, J.W. Hutchinson, N.A. Fleck, M.F. Ashby, H.N.G. Wadley, The topological design of multifunctional cellular metals, *Prog. Mater. Sci.* 46 (2001) 309–327.
- [5] A.G. Evans, M.Y. He, V.S. Deshpande, J.W. Hutchinson, A.J. Jacobsen, W.B. Carter, Concepts for enhanced energy absorption using hollow micro-lattices, *Int. J. Impact Eng.* 37 (2010) 947–959.
- [6] C.I. Hammett, R.G. Rinaldi, F.W. Zok, Pyramidal lattice structures for high strength and energy absorption, *J. Appl. Mech.* 80 (2013), 041015–041015.
- [7] T.A. Schaedler, C.J. Ro, A.E. Sorensen, Z. Eckel, S.S. Yang, W.B. Carter, A.J. Jacobsen, Designing metallic microlattices for energy absorber applications, *Adv. Eng. Mater.* 16 (2014) 276–283.
- [8] T.J. Lu, L. Valdevit, A.G. Evans, Active cooling by metallic sandwich structures with periodic cores, *Prog. Mater. Sci.* 50 (2005) 789–815.
- [9] T.A. Schaedler, A.J. Jacobsen, A. Torrents, A.E. Sorensen, J. Lian, J.R. Greer, L. Valdevit, W.B. Carter, Ultralight metallic microlattices, *Science* 334 (2011) 962–965.
- [10] A. Cao, P.L. Dickrell, W.G. Sawyer, M.N. Ghasemi-Nejhad, P.M. Ajayan, Super-compressible foaml-like carbon nanotube films, *Science* 310 (2005) 1307–1310.
- [11] V.S. Fleck, M.F. Deshpande, Micro-architected materials: past, present and future, *Proc. R. Soc. A Math. Phys. Eng. Sci.* 466 (2010) 2495–2516.
- [12] A. Torrents, T.A. Schaedler, A.J. Jacobsen, W.B. Carter, L. Valdevit, Characterization of nickel-based microlattice materials with structural hierarchy from the nanometer to the millimeter scale, *Acta Mater.* 60 (2012) 3511–3523.
- [13] L. Salari-Sharif, T.A. Schaedler, L. Valdevit, Energy dissipation mechanisms in hollow metallic microlattices, *J. Mater. Res.* 29 (2014) 1755–1770.
- [14] A.J. Jacobsen, W. Barvosa-Carter, S. Nutt, Micro-scale truss structures formed from self-propagating photopolymer waveguides, *Adv. Mater.* 19 (2007) 3892–3896.
- [15] A.J. Jacobsen, W. Barvosa-Carter, S. Nutt, Micro-scale truss structures with three-fold and six-fold symmetry formed from self-propagating polymer waveguides, *Acta Mater.* 56 (2008) 2540–2548.
- [16] L. Valdevit, S.W. Godfrey, T.A. Schaedler, A.J. Jacobsen, W.B. Carter, Compressive strength of hollow microlattices: experimental characterization, modeling, and optimal design, *J. Mater. Res.* 28 (2013) 2461–2473.
- [17] L. Salari-Sharif, L. Valdevit, Accurate stiffness measurement of ultralight hollow metallic microlattices by laser vibrometry, *Exp. Mech.* 54 (2014) 1491–1495.
- [18] S.W. Godfrey, L. Valdevit, A novel modeling platform for characterization and optimal design of micro-architected materials, in: *AIAA Struct. Dyn. Mater. Conf.*, Honolulu, HI, 2012.
- [19] X. Zheng, H. Lee, T.H. Weisgraber, M. Shusteff, DeOtte J, E.B. Duoss, J.D. Kuntz, M.M. Biener, Q. Ge, S.O. Jackson, N.X. Kucheyev, C.M. Fang, Ultralight, ultrastiff mechanical metamaterials, *Science* 344 (2014) 1373–1377.
- [20] L.R. Meza, A.J. Zelhofer, N. Clarke, A.J. Mateos, D.M. Kochmann, J.R. Greer, Resilient 3D hierarchical architected metamaterials, *Proc. Natl. Acad. Sci. U. S. A.* 112 (2015) 11502–11507.
- [21] D. Jang, L.R. Meza, F. Greer, J.R. Greer, Fabrication and deformation of three-dimensional hollow ceramic nanostructures, *Nat. Mater.* 12 (2013) 893–898.
- [22] J.C. Wallach, L.J. Gibson, Defect sensitivity of a 3D truss material, *Scr. Mater.* 45 (2001) 639–644.
- [23] N.M. Ruvalcaba, A. Ortega, A. Asadpoure, L. Valdevit, Uniaxial strength of hollow microlattices with partially cracked nodes, In Submission.
- [24] A.J. Jacobsen, W. Barvosa-Carter, S. Nutt, Compression behavior of micro-scale truss structures formed from self-propagating polymer waveguides, *Acta Mater.* 55 (2007) 6724–6733.
- [25] K.J. Maloney, C.S. Roper, A.J. Jacobsen, W.B. Carter, L. Valdevit, T.A. Schaedler, Microlattices as architected thin films: analysis of mechanical properties and high strain elastic recovery, *APL Mater.* 1 (2013) 1–8.
- [26] C.R. Calladine, *Theory of Shell Structures*, Cambridge University Press, 1983.
- [27] J.M. Teng, J.M. Rotter, *Buckling of Thin Metal Shells*, 2004.
- [28] Buckling of Thin-walled Circular Cylinder, National Aeronautic Space Administration, 1965.
- [29] C.A. Schenk, G.I. Schuëller, Buckling analysis of cylindrical shells with random geometric imperfections, *Int. J. Non Linear. Mech.* 38 (2003) 1119–1132.
- [30] V.M. Zeinoddini, B.W. Schafer, Simulation of geometric imperfections in cold-formed steel members using spectral representation approach, *Thin-Walled Struct.* 60 (2012) 105–117.
- [31] M. Tootkaboni, L. Graham-Brady, B.W. Schafer, Geometrically non-linear behavior of structural systems with random material property: an asymptotic spectral stochastic approach, *Comput. Methods Appl. Mech. Eng.* 198 (2009) 3173–3185.
- [32] H. Foroughi, C.D. Moen, A. Myers, M. Tootkaboni, L. Vieira, B.W. Schafer, Analysis and design of thin metallic shell structural members –current practice and future research needs, *Proc. Ann. Stab. Conf.* (2014).
- [33] X. Zhao, M. Tootkaboni, B.W. Schafer, Development of a laser-based geometric imperfection measurement platform with application to cold-formed steel construction, *Exp. Mech.* 55 (2015) 1779–1790.
- [34] X. Zhao, M. Tootkaboni, B.W. Schafer, Laser-based cross-section measurement of cold-formed steel members: model reconstruction and application, *Thin-Walled Struct.* 120 (2017) 70–80.
- [35] Michel Loeve, *Probability Theory*, Springer-Verlag, New York, 1978.